Targeting skeletal endothelium to ameliorate bone loss

Ren Xu[1], **Alisha Yallowitz**[1], **An Qin**[2], **Zhuhao Wu**[3], **Dong Yeon Shin**[1], **Jung-Min Kim**[4], **Shawon Debnath**[1], **Gang Ji**[5,6], **Mathias P. Bostrom**[5,7], **Xu Yang**[5], **Chao Zhang**[8], **Han Dong**[9,10], **Pouneh Kermani**[11], **Sarfaraz Lalani**[1], **Na Li**[1], **Yifang Liu**[1], **Michael G. Poulos**[11], **Amanda Wach**[12], **Yi Zhang**[1], **Kazuki Inoue**[13,14], **Annarita Di Lorenzo**[1], **Baohong Zhao**[13,14], **Jason M. Butler**[11], **Jae-Hyuck Shim**[4], **Laurie H. Glimcher**[9,10], and **Matthew B. Greenblatt**[1]

[1]Department of Pathology and Laboratory Medicine, Weill Cornell Medical College, Cornell University, New York, NY 10065, USA

[2]Department of Orthopaedics, Shanghai Key Laboratory of Orthopaedic Implant, Shanghai Ninth People's Hospital, Shanghai Jiaotong University School of Medicine, Shanghai 200011, PR China

[3]Laboratory of Brain Development and Repair, The Rockefeller University, New York, NY 10065, USA

[4]Department of Medicine/Division of Rheumatology, University of Massachusetts Medical School, Worcester 01655, MA, USA

[5]Research Division, Hospital for Special Surgery, New York

[6]Department of Joint Surgery, The Third Hospital of Hebei Medical University, Shijiazhuang, 050031, PR China

[7]Division of Adult Reconstruction and Joint Replacement, Department of Orthopaedic Surgery, Hospital for Special Surgery, New York, NY 10021, USA

[8]Institute for Computational Biomedicine, Weill Cornell Medical College, Cornell University, New York, NY 10065, USA

[9]Department of Cancer Immunology and Virology, Dana-Farber Cancer Institute and Harvard University Medical School, Boston, MA 02215, USA

*To whom correspondence should be addressed. Matthew B. Greenblatt, Dept. of Pathology and Laboratory Medicine, Weill Cornell Medical College, 1300 York Ave. LC929a, New York, NY 10065 and Laurie H. Glimcher, Dana Farber Cancer Institute, Office of the President and CEO, 450 Brookline Ave, Boston, MA 02215., Tel.: 212-746-2078; Fax: 212-746-9215; mag3003@med.cornell.edu and Laurie_Glimcher@dfci.harvard.edu.

[10]Department of Medicine, Harvard Medical School and Brigham and Women's Hospital, Boston, MA 02215, USA

[11]Department of Medicine, Division of Regenerative Medicine, Ansary Stem Cell Institute, Weill Cornell Medical College, Cornell University, New York, NY 10065, USA

[12]Department of Biomechanics, Hospital for Special Surgery, New York, NY 10021, USA

[13]Arthritis and Tissue Degeneration Program and David Z. Rosensweig Genomics Research Center, Hospital for Special Surgery, New York, NY 10021, USA

[14]Department of Medicine, Weill Cornell Medical College, Cornell University, New York, NY 10065, USA

Abstract

Recent studies have identified a specialized subset of CD31^{hi}EMCN^{hi} vascular endothelium that positively regulates bone formation. However, it remains unclear how CD31^{hi}EMCN^{hi} endothelium levels are coupled to anabolic bone formation. Mice with an osteoblast-specific deletion of *Shn3*, which have markedly elevated bone formation, demonstrated an increase in CD31^{hi}EMCN^{hi} endothelium. Transcriptomic analysis identified SLIT3 as an osteoblast-derived, SHN3-regulated proangiogenic factor. Genetic deletion of *Slit3* reduced skeletal CD31^{hi}EMCN^{hi} endothelium, resulted in low bone mass due to impaired bone formation and partially reversed the high bone mass phenotype of *Shn3*$^{-/-}$ mice. This coupling between osteoblasts and CD31^{hi}EMCN^{hi} endothelium is essential for bone healing, as shown by defective fracture repair in SLIT3-mutant mice and enhanced fracture repair in SHN3-mutant mice. Finally, administration of recombinant SLIT3 both enhanced bone-fracture healing and counteracted bone loss in a mouse model of postmenopausal osteoporosis. Thus, drugs that target the SLIT3 pathway may represent a new approach for vascular-targeted osteoanabolic therapy to treat bone loss.

Keywords

Osteoblasts; skeletal fracture; vascular endothelium; osteoporosis; SLIT3

It is increasingly appreciated that the ancillary cell types present in bone tissue actively participate in osteogenesis. For example, a subset of CD31^{hi}, endomucin^{hi} (EMCN^{hi}) vascular endothelium has been recently identified as residing in the bone marrow (BM) near the growth plate. CD31^{hi}EMCN^{hi} endothelium is believed to actively direct bone formation, as alterations in CD31^{hi}EMCN^{hi} endothelium impact bone architecture, bone formation, and numbers of osteoprogenitors present in the marrow[1,2]. CD31^{hi}EMCN^{hi} endothelium levels can be altered by platelet-derived growth factor type BB (PDGF-BB), providing a potential link between bone resorption activity by osteoclasts and CD31^{hi}EMCN^{hi} endothelium[3]. However, it is currently unclear if and how levels of CD31^{hi}EMCN^{hi} endothelium are coupled with the physiologic need for bone formation and whether osteoblasts participate in this regulation.

Previously, we demonstrated that the adaptor protein Schnurri3 (SHN3) is a suppressor of osteoblast activity, as mice lacking SHN3 display a progressive increase in postnatal bone

mass due to augmented bone formation[4,5]. As deletion of *Shn3* in osteoblast-lineage cells is sufficient to greatly enhance bone formation, it appears that osteoblasts are able to coordinate all of the various tissue activities beyond osteoblast-mediated matrix secretion needed to form mature bone. Given the substantial osteoblast-intrinsic augmentation of bone formation in SHN3-deficient mice, we believed that this mouse strain represented an ideal opportunity to study how osteoblasts induce changes in their supporting cell lineages to facilitate bone formation.

Here we show that CD31^{hi}EMCN^{hi} skeletal vasculature is present at higher levels in mice with an inducible deletion of *Shn3* in osteoblasts and demonstrate that CD31^{hi}EMCN^{hi} endothelium is regulated by osteoblasts. We further identify the secreted ligand SLIT3 as a novel SHN3-controlled, osteoblast-derived regulator of CD31^{hi}EMCN^{hi} endothelium levels. SLIT3 belongs to a conserved family of 3 SLIT ligands that were initially discovered in the context of CNS development, where they mediate axonal guidance through ROBO receptors (Robo1-4)[6,7]. Subsequent studies showed SLITs are widely expressed, and the SLIT/ROBO pathway has been implicated in multiple physiological functions outside of the nervous system such as angiogenesis/vasculogenesis[8–10], stem cell regulation[11,12] and cancer development[13]. Additionally, SLIT3 has been identified as a proangiogenic factor in mouse models and human engineered tissue[14,15]. However, the role of SLIT3 in bone metabolism is still largely unclear.

Results

SHN3 acts in osteoblasts to regulate CD31^{hi}EMCN^{hi} endothelium

To address our hypothesis that osteoblasts are able to coordinate levels of osteogenic CD31^{hi}EMCN^{hi} endothelium to maintain bone formation capacity, we assessed CD31^{hi}EMCN^{hi} endothelium levels in a mouse strain displaying augmented postnatal bone formation – namely, *Shn3*$^{-/-}$ mice. We found that CD31, EMCN-double positive endothelium was present in the marrow immediately beneath the growth plate and was significantly higher in *Shn3*$^{-/-}$ mice relative to WT controls. This effect was bone-specific as, relative to littermate controls, *Shn3*$^{-/-}$ mice displayed normal levels of EMCN-positive vessels in other organs including heart, brain, lung and kidney (Supplementary Fig. 1a). This vessel phenotype was present in neonatal *Shn3*$^{-/-}$ mice and thus preceded the appearance of the high bone mass phenotype[5] (Supplementary Fig. 1b). Flow cytometry also confirmed greater amounts of CD31^{hi}EMCN^{hi} vascular endothelium in the bones of *Shn3*$^{-/-}$ mice relative to WT littermate controls (Fig. 1e–f **and** Supplementary Fig. 1c). Taken together, these observations suggest that SHN3 regulates levels of skeletal CD31^{hi}EMCN^{hi} endothelium in addition to its role in regulating osteoblast activity.

As SHN3 acts in a cell intrinsic manner to regulate bone formation by osteoblasts, we reasoned that SHN3 also acts in osteoblasts to control levels of CD31^{hi}EMCN^{hi} endothelium. To test this directly, we bred *Shn3*$^{f/f}$ mice to a cre-deleter strain targeting osteoblast progenitors, OSX-cre, and to a cre-deleter strain targeting mature osteoblasts, DMP1-cre. Both *Shn3*^{osx} and *Shn3*^{dmp1} male mice exhibited a similar degree of higher bone mass relative to littermate *Shn3*$^{f/f}$ controls, including greater cortical bone thickness, largely recapitulating the characteristic bone phenotype of *Shn3*$^{-/-}$ mice (Fig. 2a, b and

Supplementary Fig. 2a–c). Based on this, we selected the *Shn3*[dmp1] strain was selected for further study as it implicates a more restricted subpopulation in any phenotypes observed[16,17]. Histomorphometric analysis confirmed that the high bone mass phenotype of *Shn3*[dmp1] mice was due to augmented osteoblast-mediated bone formation predominantly on the endosteal surface (Fig. 2c, d and Supplementary Fig. 2d, e). Analysis of skeletal CD31^{hi}EMCN^{hi} endothelium by both immunostaining and flow cytometry demonstrated that *Shn3*[dmp1] mice displayed higher levels of this subset of endothelial cells relative to littermate *Shn3*[f/f] controls in a similar manner as seen in *Shn3*^{−/−} mice (Fig. 2e–g and Supplementary Fig. 2f–h).

To further confirm that the function of SHN3 to regulate skeletal CD31^{hi}EMCN^{hi} vascular endothelium maps to osteoblasts, we generated endothelial cell-specific Shn3-deficient mice (*Shn3*[cdh5] mice) using the Cdh5 (VE-cadherin)-Cre. Despite observing efficient deletion of *Shn3* in BM endothelial cells (Supplementary Fig. 2i), levels of CD31^{hi}EMCN^{hi} endothelial cells were unchanged in *Shn3*[cdh5] mice relative to littermate *Shn3*[f/f] controls (Supplementary Fig. 2j–m). Accordingly, *Shn3*[cdh5] mice also displayed normal bone mass relative to littermate *Shn3*[f/f] controls (Supplementary Fig. 2n). Taken together with the *Shn3*^{−/−} and *Shn3*[dmp1] phenotype, we conclude that osteoblasts regulate skeletal CD31^{hi}EMCN^{hi} vascular endothelium in a SHN3-dependent manner, and that SHN3 does not act directly in endothelial cells to regulate skeletal phenotypes.

To determine if osteoblasts continuously participate in this regulation or if this process is limited to embryonic development, we intercrossed *Shn3*[f/f] mice with osteocalcin-CreERT mice expressing a tamoxifen-activated Cre recombinase in mature osteoblasts under the control of the osteocalcin promoter (*Shn3*[ocn-ert] mice). Cre-mediated deletion was induced with tamoxifen, and the resulting skeletal and vascular phenotypes were analyzed. Relative to either tamoxifen treatment of *Shn3*[f/f] mice, tamoxifen treatment of *Shn3*[ocn-ert] mice resulted in higher levels of both CD31^{hi}EMCN^{hi} endothelial cells and trabecular bone mass and cortical bone thickness, with the change in CD31^{hi}EMCN^{hi} endothelium preceding detectable effects on bone mass (Fig. 2h–l and Supplementary Fig. 2o). Thus, mature osteoblasts continuously participate in tuning the levels of CD31^{hi}EMCN^{hi} endothelium in bone, and this coupling is not solely a developmental phenomenon.

SHN3 regulates *Slit3* expression in osteoblasts

To investigate if the regulation of marrow angiogenesis by SHN3 is a direct effect of osteoblasts on endothelial cells, conditioned medium was harvested from WT and *Shn3*^{−/−} primary osteoblasts and introduced to cultures of primary bone marrow-derived endothelial cells. Conditioned medium from *Shn3*^{−/−} primary osteoblasts displayed an enhanced ability relative to conditioned medium from WT osteoblasts to induce endothelial migration and capillary tube formation, suggesting that the relevant mediator is a soluble osteoblast-derived factor (Fig. 3a–d). To identify potential proangiogenic factors regulated by SHN3 in osteoblasts, we performed RNA sequencing transcriptional profiling. Gene ontology (GO) analysis demonstrated that the set of differentially expressed genes in *Shn3*^{−/−} versus WT osteoblasts is enriched for genes mediating angiogenesis in addition to the expected enrichment for genes involved with bone development and mineralization (Fig. 3e).

Examination of the expression of a number of proangiogenic factors revealed that only SLIT3, a soluble axonal chemorepellent recently shown to have angiogenic functions, showed substantially higher levels in *Shn3*^{-/-} osteoblasts (Fig. 3f)[3,14]. Further expression analysis confirmed robust *Slit3* expression in osteoblasts and demonstrated negligible *Slit3* expression in osteoclasts (Supplementary Fig. 3a, b)[18]. Similarly, immunofluorescence for beta-galactosidase in *Slit3*^{+/-} mice[19] bearing a targeted insertion of a LacZ cassette into the *Slit3* locus identified SLIT3 expression in cells adjacent to the bone surface consistent with osteoblasts (Supplementary Fig. 3c). Similarly, human mesenchymal stromal cell-derived osteoblasts also expressed *Slit3* (Supplementary Fig. 3d). To verify that *Slit3* expression is augmented in *Shn3*^{-/-} osteoblasts relative to WT controls, we utilized three complimentary approaches. First, real-time PCR was used to validate the higher levels of *Slit3* observed by RNA sequencing (Fig. 3g). Second, overexpression or knockdown of *Shn3* in human mesenchymal stem cell (hMSC)-derived osteoblasts demonstrated, respectively, a suppression or an enhancement of both mRNA and protein levels of *Slit3* (Fig. 3h, i). Moreover, overexpression of *Shn3* in murine primary osteoblasts also dramatically reduced SLIT3 expression (Supplementary Fig. 3e). Lastly, ELISA demonstrated 3-fold higher SLIT3 secretion in conditioned medium from *Shn3*^{-/-} osteoblasts relative to WT controls (Fig. 3j). Thus, SHN3 is a negative regulator of SLIT3 expression in osteoblasts.

Recent studies have shown that preosteoclast-derived PDGF-BB is able to induce CD31^{hi}EMCN^{hi} endothelium in bone[3]. We were unable to detect PDGF-BB secretion by osteoblasts, and negligible *Pdgfb* mRNA was observed in both WT and *Shn3*^{-/-} osteoblasts (Fig. 3f and Supplementary Fig. 3f). In addition, serum PDGF-BB levels were unaltered in *Shn3*^{-/-} mice (Supplementary Fig. 3f). Thus, we do not observe evidence of regulation of PDGF-BB by SHN3.

SHN3 acts predominantly by regulating ERK activity, as mice bearing a knockin of a mutation in 3 amino acids comprising the ERK interacting motif (*Shn3*[KI/KI] mice) in SHN3 largely recapitulate the high bone mass phenotype of *Shn3*^{-/-} mice[4]. *Slit3* levels were also higher in in primary *Shn3*[KI/KI] osteoblasts relative to WT controls (Fig. 3k), and treatment with the ERK pathway inhibitor trametinib reduced *Slit3* expression in both hMSC-derived osteoblasts and murine primary calvarial osteoblasts relative to vehicle (Fig. 3l and Supplementary Fig. 3g). Consistent with these observations, *Shn3*[KI/KI] mice also displayed higher levels of CD31^{hi}EMCN^{hi} skeletal endothelium, a phenotype similar to that seen in *Shn3*^{-/-} mice (Fig. 3m). Thus, SHN3 regulates SLIT3 expression and CD31^{hi}EMCN^{hi} endothelium levels via its ability to bind and regulate ERK.

SLIT3 acts downstream of SHN3 to promote CD31^{hi}EMCN^{hi} endothelium formation and bone formation *in vivo*

To determine if SLIT3 contributes to the regulation of BM endothelium by osteoblasts *in vitro,* we conducted a dose response curve for SLIT3 treatment as described in prior studies[14,20,21]. BM endothelial progenitor outgrowth cells (EPOCs) treated with recombinant SLIT3 displayed enhanced migration and tube formation relative to a vehicle control (Fig. 4a, b and Supplementary Fig. 4a). Additionally, SLIT3 resulted in modestly higher levels of proliferation in BM derived EPOCs, consistent with the activity of SLIT3

observed in non-skeletal vascular endothelium[14] (Supplementary Fig. 4b). SLIT1 and SLIT2 displayed a similar ability to promote tube formation relative to vehicle, consistent with observations that each of the SLITs displays a similar capacity for ROBO binding and activation[9,22,23] (Supplementary Fig. 4c, d). Next, conditioned medium was collected from WT and *Shn3*^{−/−} osteoblasts and placed on BM derived endothelial cells together with an anti-SLIT3 blocking antibody or an isotype control. Enhanced tube formation was seen with conditioned medium from SHN3-deficient osteoblasts, and treatment with an anti-SLIT3 blocking antibody abrogated this effect (Fig. 4c, d). Investigation of the signaling pathways downstream of SLIT3 in BM endothelial cells demonstrated activation of ERK MAPK and Hippo signaling, pathways known to participate in angiogenesis (Supplementary Fig. 4e)[24,25]. Interestingly, we also noted that treatment of BM-derived endothelial cells with SLIT3 enhanced the acquisition of a CD31^{hi}EMCN^{hi} surface immunophenotype in culture (Supplementary Fig. 4f). Similarly, systemic administration of SLIT3 resulted in higher levels of skeletal CD31^{hi}EMCN^{hi} endothelium production *in vivo* (Supplementary Fig. 4g). In addition, SLIT2 augmented formation of CD31^{hi}EMCN^{hi} endothelium *in vivo* relative to vehicle, suggesting that other SLITs are also capable of eliciting this response (Supplementary Fig. 4h). Thus, SLIT3 is both necessary and sufficient to mediate osteogenesis by regulating production of CD31^{hi}EMCN^{hi} endothelium.

To assess if SLIT3 regulates CD31^{hi}EMCN^{hi} endothelium under physiologic conditions, immunofluorescence and flow cytometry were performed on *Slit3*^{−/−} mice, with both approaches revealing a reduction in CD31^{hi}EMCN^{hi} skeletal endothelium (Fig. 4e–h). Concurrent with this reduction in CD31^{hi}EMCN^{hi} endothelium, *Slit3*^{−/−} mice showed a substantial reduction in both total bone mass and cortical bone thickness relative to WT littermates (Fig. 4i–k). Consistent with prior reports[19], *Slit3*^{−/−} mice displayed a decrease in body weight at 1 month of age, with body weight normalization occurring by 3 months of age (Supplementary Fig. 5a). Thus, osetopenia could be observed even at ages where the weight of *Slit3*^{−/−} mice was indistinguishable from that of littermate controls. This osteopenia was due to reduced osteoblast activity, as bone formation was reduced without significant alterations in osteoclast numbers or serum CTX, a marker of osteoclast activity (Fig. 4l, m and Supplementary Fig. 5b, c). To evaluate if this reduction in bone formation was due to cell intrinsic defects in osteoblast activity, we examined the differentiation of SLIT3-deficient osteoblasts. Mineralization activity, ALP induction, and induction of characteristic osteoblast transcripts were all intact or even slightly enhanced in the absence of SLIT3 (Supplementary Fig. 5d–f). Furthermore, treatment of osteoblasts with recombinant SLIT3 did not enhance osteoblast activation relative to vehicle, nor did treatment with a ROBO1-Fc fusion that blocks SLIT signaling impair osteoblast differentiation (Supplementary Fig. 5g, h). Thus, the ability of SLIT3 to enhance bone formation *in vivo* is not attributable to the direct effects of SLIT3 on osteoblasts, consistent with the model that SLIT3 directly augments levels of CD31^{hi}EMCN^{hi} endothelium to augment bone formation. To confirm if osteoblasts represent the key cellular source of SLIT3 controlling levels of skeletal CD31^{hi}EMCN^{hi} endothelium and bone mass accrual *in vivo*, mice bearing a conditional *Slit3* floxed allele (*Slit3*[f/f] mice) were generated, and their deletion capacity was validated (Supplementary Fig. 6a). We bred *Slit3*[f/f] mice to cre-deleter strains targeting either osteoblast progenitors via OSX-cre or mature osteoblasts via DMP1-

cre. Osteoblast-specific deletion of *Slit3 in vivo* recapitulated both the impaired CD31^{hi}EMCN^{hi} endothelium levels and the osteopenia phenotypes observed in *Slit3*^{−/−} mice (Fig. 5a–d and Supplementary Fig. 6b–e). Furthermore, neither neuron-specific deletion of *Slit3* by using Synapsin-cre nor specific deletion of *Slit3* in endothelial cells by using Cdh5-cre *in vivo* led to detectable bone loss (Supplementary Fig. 6f, g). Thus, osteoblasts are the key functional source of SLIT3 influencing skeletal biology.

We next questioned whether the enhanced production of SLIT3 by SHN3-deficient osteoblasts contributes to the high bone mass phenotype of SHN3-deficient mice. To address this, a genetic interaction study was performed by intercrossing *Shn3*^{−/−} and *Slit3*^{−/−} mice. As shown in Fig. 4, an epistatic genetic interaction was observed between *Shn3*- and *Slit3*-null alleles, as the higher bone formation, trabecular bone mass, and CD31^{hi}EMCN^{hi} endothelial cell levels in *Shn3*^{−/−} mice were partially reversed in *Shn3*^{−/−} *Slit3*^{−/−} mice. Thus, SLIT3 contributes to both the high bone mass phenotype and enhanced CD31^{hi}EMCN^{hi} endothelium phenotype of SHN3-deficient mice *in vivo*. In addition, a genetic interaction similar to that observed with the *Shn3* and *Slit3* germline null alleles was recapitulated using conditional deletion of *Shn3* and *Slit3* alleles in osteoblasts using Osx-cre (Supplementary Fig. 7a, b). Thus, the interaction between *Shn3* and *Slit3* alleles to regulate bone mass is intrinsic to osteoblasts. Taken together, these results imply that SLIT3 production is utilized by osteoblasts to condition their environment through angiogenesis to be conducive for bone formation.

ROBO1 is a key receptor for SLIT3 on marrow endothelial cells

As SLITs are known to signal through the Roundabout family (ROBO1-4) of receptors, we next explored which ROBO receptors might be acting in endothelial cells to mediate the response to SLIT3[26]. CD31^{hi}EMCN^{hi} skeletal endothelial cells were isolated by FACS and subjected to RNA-seq transcriptome analysis, revealing that *Robo1* and *Robo4* are the predominant ROBO family receptors expressed (Supplementary Fig. 8a). Immunofluorescence for beta-galactosidase in the bones of *Robo1*^{+/−} mice bearing a knockin of a LacZ cassette into the *Robo1* locus confirmed that *Robo1* expression is present in endothelium near the growth plate, a localization consistent with CD31^{hi}EMCN^{hi} endothelial cells (Supplementary Fig. 3c). We also characterized ROBO expression in other skeletal cell types, indicating that osteoblasts express *Robo1* and *Robo2* whereas osteoclasts show negligible expression of ROBO family members. (Supplementary Fig. 8b, c). Given the expression of *Robo1* and *Robo4* in CD31^{hi}EMCN^{hi} endothelial cells, the skeletal phenotype of *Robo1*^{−/−} and *Robo4*^{−/−} mice was examined. *Robo1*^{−/−} but not *Robo4*^{−/−} mice display low trabecular bone mass in long bones relative to WT controls (Fig. 5e and Supplementary Fig. 8d, e), and *Robo1*^{−/−} mice also showed lower levels of CD31^{hi}EMCN^{hi} skeletal endothelium (Fig. 5f and Supplementary Fig. 8f). *Robo2* expression was not detected in either sorted CD31^{hi}EMCN^{hi} skeletal endothelial cells or cultured BM derived endothelial cells, and *Robo2* expression was not induced by either germline *Robo1*-deficiency or shRNA-mediated *Robo1* knockdown. (Supplementary Fig. 8g–i). Thus, no evidence of ROBO2-medaited compensation for ROBO1 loss-of-function was observed.

Next, the mechanism of SLIT3 mediated effects on BM endothelial cells was investigated. Knockdown of *Robo1* in BM derived endothelial cells impaired their response to SLIT3 relative to an irrelevant shRNA control as determined by both their tube formation capacity and phosphorylation of the hippo pathway signaling intermediate YAP (Supplementary Fig. 9a, b). YAP has been reported to play a crucial role endothelial cell migration and tube formation[25,27]. Consistent with this, relative to an irrelevant shRNA control, shRNA-mediated knockdown of YAP significantly reduced the ability of SLIT3 but not FGF2 to induce tube formation in BM-derived endothelial cells, indicating that YAP acts downstream of the SLIT3/ROBO1 pathway to control tube formation (Supplementary Fig. 9c, d). Taken together, ROBO1 is a key receptor controlling both endothelial cell responses to SLIT3 and overall bone mass accrual.

A SHN3/SLIT3 osteoblast-endothelium coupling pathway plays an essential role in fracture healing

Given that bone repair is accompanied by extensive elaboration of new blood vessels, we hypothesized that the SHN3/SLIT3 pathway mediated communication between osteoblasts and endothelial cells may be vital for bone fracture healing. In support of this hypothesis, immunohistochemical analysis of human fracture callus tissue demonstrated robust expression of SLIT3 in osteoblasts and the presence of CD31$^+$ endothelium in physical proximity to osteoblasts (Supplementary Fig. 10a, b). An open femoral midshaft fracture model was established and used to study bone healing in *Shn3*$^{-/-}$, *Slit3*$^{-/-}$, *Shn3*$^{-/-}$ *Slit3*$^{-/-}$ and WT control mice. 21 days post-fracture, we performed μCT and histology analysis and found that fracture healing was enhanced in *Shn3*$^{-/-}$ mice. Relative to WT controls, the fracture site in *Shn3*$^{-/-}$ mice displayed extensive bridging with mature lamellar bone that had already remodeled to contain marrow elements within the newly formed callus tissue. In contrast, deletion of *Slit3* led to complete non-union and arrest of fracture healing with only trace amounts of cartilaginous callus present relative to WT controls (Fig. 6a–c). Consistent with the results of the bone mass genetic interaction studies, SLIT3 deficiency largely reversed the enhanced healing phenotype of SHN3-deficient mice. These observations of enhanced and impaired healing in SHN3-deficient and SLIT3-deficient mice, respectively, translated into improved or impaired biomechanical properties of the callus, as shown by the load to failure or maximum load sustained across the fracture site. Consistent with observations in basal bone mass phenotypes, *Shn3*$^{-/-}$ mice displayed enhanced angiogenesis throughout the callus relative to WT controls, and this phenotype was reversed by SLIT3 deficiency (Fig. 6d, e and Supplementary Fig. 10c, d). Thus, the coupling between osteoblasts and vascular endothelium mediated by the SHN3/SLIT3 pathway is essential for fracture healing.

SLIT3 has therapeutic effects in models of fracture healing and postmenopausal osteoporosis

As SLIT3 mediated crosstalk between osteoblasts and CD31^{hi}EMCN^{hi} endothelium is an important regulator of bone mass accrual and bone-fracture healing, we hypothesized that administration of exogenous SLIT3 may have therapeutic effects to promote bone formation and regeneration. To examine this, we administered recombinant SLIT3 twice weekly via i.v. injection in 5-week-old male mice concurrent with performing an open femoral midshaft

fracture. After 21 days of treatment, μCT and histological analysis showed an enhancement of bone fracture healing in SLIT3-treated mice (Fig. 6f, g). The bone volume in the callus area was greater by almost 2-fold relative to controls (Fig. 6h). Furthermore, vascularization of the fracture callus was also augmented by SLIT3 administration relative to vehicle (Fig. 6i and Supplementary Fig. 10e). Finally, biomechanical testing demonstrated that SLIT3 treatment significantly enhanced the maximum load sustained and stiffness of the fracture callus, demonstrating improvements in clinically meaningful endpoints (Fig. 6j). Notably, examination of vascular morphology did not detect alterations in lung, heart, kidney or retina, and no changes in brain ultrastructure were present after SLIT3 administration (Supplementary Fig. 11a–d). Thus, under this dosing strategy and with regards to these endpoints, the effects of SLIT3 were specific to bone.

Nevertheless, because SLIT3 can affect a wide variety of tissues, it is important to anticipate potential extra-skeletal toxicities of SLIT3 therapy. As a proof-of-principle strategy to avoid potential extra-skeletal toxicities, local delivery of SLIT3 into a fracture site was achieved with a SLIT3-loaded collagen sponge. This approach recapitulated the effects of systemic SLIT3 delivery in promoting fracture healing as judged by improved mineralization and biomechanical properties of the fracture callus and augmented formation of $CD31^{hi}EMCN^{hi}$ endothelium relative to either no sponge or implantation of a sponge without SLIT3 (Fig. 6k, l and Supplementary Fig. 11e). Local delivery of SLIT3 also did not impact non-skeletal vascular abundance or morphology or brain ultrastructure (Supplementary Fig. 11f–h).

Given the therapeutic effects of SLIT3 in a fracture model, we next examined whether systemic SLIT3 administration can protect from bone loss in the murine ovariectomy (OVX) model of postmenopausal osteoporosis[28]. Successful OVX was confirmed two months after OVX by the presence of both osteopenia and uterine atrophy (Fig 6m and Supplementary Fig. 12a, b). First, the ability of SLIT3 to prevent bone loss was examined in this model. Mice were treated with i.v. injection of SLIT3 or vehicle twice weekly initiated two weeks after OVX. Micro-CT analysis showed that SLIT3 administration significantly countered OVX-induced bone loss as shown by greater trabecular BV/TV and cortical thickness (Fig. 6m and Supplementary Fig. 12c). As the effects of SLIT3 were comparable to the effects of PTH treatment, this suggests that the magnitude of SLIT3 effect is clinically significant. Moreover, both SLIT3 and PTH administration reversed the attenuation of endosteal $CD31^{hi}EMCN^{hi}$ endothelium occurring after OVX and similarly rescued endosteal bone formation (Supplementary Fig. 12d–f). To further investigate the therapeutic activity of SLIT3, the ability of SLIT3 to promote bone formation after the onset of OVX-induced osteopenia was examined. Mice were treated with i.v. injection of SLIT3 or vehicle twice weekly initiated eight weeks after OVX surgery. SLIT3 administration significantly reversed bone loss as shown by greater trabecular BV/TV and cortical thickness (Supplementary Fig. 12g, h). Furthermore, SLIT3 administration significantly augmented the amount of $CD31^{hi}EMCN^{hi}$ endothelial cells in this context (Supplementary Fig. 12i, j). Taken together, these results provide proof-of-principle that SLIT3 may have clinical utility to enhance fracture healing and to treat disorders of low bone mass such as postmenopausal osteoporosis.

Discussion

Though bone formation is mediated solely by osteoblasts, it is likely that many other tissue types present in bone, such as vascular endothelium or autonomic and sensory nerves, contribute to creating a conducive milieu for bone formation[1,2,29–31]. To the degree that the creation of a local osteogenic milieu should be coordinated with the cell intrinsic matrix production capacity of osteoblasts, it would be mechanistically attractive for osteoblasts to regulate their own matrix production alongside the activities of these supporting cell types. However, this remains a poorly understood facet of bone physiology. Here, we hypothesized that mice with extreme increases in bone formation represent an opportunity to identify how osteoblasts regulate supporting tissue types in bone to create a pro-osteogenic milieu. In particular, we utilized the greatly enhanced bone formation phenotype of mice lacking the adaptor protein SHN3 to identify that osteoblast-derived SLIT3 enhances levels of an osteogenic subtype of vascular endothelium in bone, CD31^{hi}EMCN^{hi} endothelium. Accordingly, mice lacking SLIT3 or the known SLIT receptor ROBO1 display reduction in both the levels of marrow CD31^{hi}EMCN^{hi} endothelium and basal bone mass.

Support for osteoblasts being a key source of SLIT3 in bone include the observation of robust and specific SLIT3 expression in osteoblasts, without appreciable SLIT3 expression in osteoclasts or CD31^{hi}EMCN^{hi} endothelium. Conditional deletion of *Shn3* in late-stage osteoblasts enhanced SLIT3 expression and CD31^{hi}EMCN^{hi} endothelium levels, and osteoblast derived conditioned medium enhanced BM endothelial tube formation in a SLIT3-dependent manner. Moreover, genetic interaction studies demonstrated that the CD31^{hi}EMCN^{hi} endothelium-promoting and enhanced bone formation effects of SHN3 deficiency are partially SLIT3 dependent. This rescue of the SHN3 phenotype is not a generic property of crossing SHN3 to a mouse with low bone mass, as crossing the *Shn3*$^{-/-}$ mouse strain to the osteopenic *Rsk2*$^{-/-}$ strain did not significantly alter the Shn3$^{-/-}$ phenotype [4]. Thus, the epistatic interaction between *Shn3* and *Slit3* alleles in both regulation of bone mass and CD31^{hi}EMCN^{hi} endothelium levels provides in vivo genetic evidence that SLIT3 is a critical effector downstream of SHN3, though it does not preclude the existence of additional effectors.

Additionally, ROBO1-deficient but not ROBO4-deficient mice show an osteopenic phenotype, and accordingly ROBO1 knockdown partially blocks BM endothelial responses to SLIT3. Though the phenotype of ROBO1-deficient mice and the in vitro studies indicate that it is a key receptor of SLIT signals in the regulation of bone mass accrual, it cannot be excluded that other SLIT/ROBO members similarly contribute in either an independent or redundant manner[26].

Flow cytometry analysis of CD31^{hi}EMCN^{hi} endothelium suggests that this is a relatively rare population of cells, with only very limited numbers of cells present relative to other hematopoietic or mesenchymal lineages. This raises the question of how such a small population can exert such a large effect on organ physiology. One possible explanation is that the highest density of CD31^{hi}EMCN^{hi} endothelium is observed at very active sites of bone formation, such as the primary spongiosum immediately adjacent to the growth plate of an actively growing long bone, and within this site CD31^{hi}EMCN^{hi} endothelium is observed

to be in close physical proximity with osteoblast-lineage cells. This physical proximity between CD31^{hi}EMCN^{hi} endothelium and the osteoblast lineage cells they support may act to amplify each other's physiologic effects. Further work is needed to clarify the nature and mediators of these interactions beyond SLIT3. Additionally, much remains to be learned about properties that define CD31^{hi}EMCN^{hi} endothelium, including how this population relates to other endothelial cell types present in bone[32].

Given the evidence that fracture healing is accompanied by extensive elaboration of new blood vessels, the role of SHN3/SLIT3 mediated coupling between osteogenesis and CD31^{hi}EMCN^{hi} endothelium was explored in bone regeneration and found to be critically important. Impaired fracture healing is observed in elderly patients, patients with systemic vascular diseases such as diabetes, patients with inflammatory disorders or chronic infection, or in patients with large traumatic bone defects[33]. For these classes of patients, a single bone fracture often results in many years of pain, severely impaired mobility and numerous attempts at surgical management of their fracture. From this perspective, developing a means for medical therapy to promote fracture healing is urgently needed. Interestingly, the phenotypes observed with disruption of the SHN3/SLIT3 axis may extend beyond simply promoting more bone formation, as the fracture callus observed in SHN3-deficient mice was markedly more mature, including displaying overall more mature lamellar bone in addition to enhanced recruitment of hematopoietic elements to the callus. Conversely, SLIT3-deficient mice displayed an arrest at early stages of fracture callus maturation, displaying a lack of propagation of the mineralization sites on either side of the callus.

Here we also provide proof-of-principle for the potential of exogenous SLIT3 to promote bone fracture healing and prevent bone loss in a model of postmenopausal osteoporosis. Notably, these findings contrast with a prior in vitro study suggesting that SLIT2 suppresses osteoblast differentiation *in vitro* [34]. This result more broadly suggests that agents targeting bone vasculature may represent a novel class of bone anabolics and raises the possibility that vascular-targeted anabolics may have a synergistic or complimentary effect when used in combination with an osteoblast-targeted anabolic such as a PTH analogue or an anti-SOST antibody. Development of new categories of bone anabolic agents is especially important given the current limitations on the maximum duration of therapy with PTH-based anabolic agents. Likewise, in light of increasing evidence establishing that osteoporosis drugs can be used in a sequential or combination manner to obtain superior clinical outcomes, having therapeutic access to a larger diversity of anabolic pathways is highly desirable[35]. Notably, as the pharmacokinetics and pharmacodynamics of SLIT3 *in vivo* are not currently known, further enhancement of the magnitude of SLIT3 effect may be possible with optimization of dosing and delivery strategies.

Online Methods

Genetically modified mice

Shn3^{−/−} (BALB/c), *Shn3*[KI/KI] (C57BL/6j), *Shn3* floxed allele (C57BL/6j), *Slit3*^{−/−} (BALB/c), *Robo1*^{−/−} (ICR) and *Robo4*^{−/−} (C57BL/6j) mice were all previously reported, with *Robo1*^{−/−} mice being a generous gift from Dr. Marc Tessier-Lavigne [4,7,8,14,19,36]. To generate *Slit3* floxed mice, the SLIT3-F08 mouse embryonic stem (ES) cell line in which

exon 8 is flanked by *loxP* sites was obtained from International Mouse Phenotyping Consortium (IMPC). After validation, F08 EC cells were injected into C57BL/6J blastocysts, and the derived chimeras displaying germline transmissions were selected for further breeding. The LacZ and neo cassettes were removed by intercrossing with transgenic mice expressing Flp recombinase. *Slit3* floxed mice were backcrossed with C57BL/6j mice for 8 generations.

Transgenic mice expressing Cre recombinase under control of the cdh5 promoter (cdh5-Cre) [37], osterix promoter (osx-Cre) [38], dmp1 promoter (dmp1-Cre) [39] and Osteocalcin-CreERT mice[40] were mated with *Shn3* floxed mice or *Slit3* floxed mice to obtain various *Shn3 or Slit3* conditional KO mouse. For postnatal activation of CreERT, 100mg/kg tamoxifen (Sigma) in corn oil (Sigma) was intraperitoneally injected to 1 month-old mice once a day for five consecutive days. Littermate controls were utilized for all experiments. All animals were maintained in accordance with the National Institutes of Health Guide for the Care and Use of Laboratory Animals and were handled according to protocols approved by the Weill Cornell Medical College subcommittee on animal care (IACUC).

µCT Analysis

µCT analysis was conducted on a Scanco Medical µCT 35 system at the Citigroup Biomedical Imaging Core using the previously described parameters[4]. µCT analysis was performed by an investigator blinded to the genotypes of the animals under analysis.

Immunofluorescence, histology and histomorphometry

For immunofluorescence, fresh bone dissected and soft tissues from wild-type mice and mutant mice were collected and immediately fixed in ice-cold 4% paraformaldehyde solution for overnight. Decalcification was specially carried out with 0.5 M EDTA at 4°C with constant shaking for bone samples from mice (age   1W). All samples were embedded in OCT compound (Sakura) and cut into 25-um-thick sagittal sections using a cryostat (Leica). Immunofluorescence staining and analysis was performed as described previously[29,41]. Briefly, after treatment with 0.2% Triton X-100 for 10 min, sections were blocked with 5% donkey serum at room temperature for 30 min and incubated overnight at 4°C with antibodies: CD31 (553370, BD Pharmigen, 1:100), CD31 conjugated to Alexa Fluor 488 (FAB3628G, R&D Systems, 1:50), Endomucin (sc-65495, Santa Cruz, 1:100), Neurofilament M Antibody (841001, Biolegend) or Beta Galactosidase antibody (GTX77365, Gene Tex, 1:100). Primary antibodies were visualized with species appropriate Alexa Fluor-coupled secondary antibodies (1:400, Molecular Probes). Nuclei were counterstained with DAPI. Brian sections also were stained by Red Fluorescent Nissl (Thermo). All immunofluorescence experiments were confirmed by at least one independent repeat. An Olympus IX81 confocal microscope or Zeiss LSM-880 confocal microscope was used to image samples. Quantification of skeletal vasculature was performed as previously described[29]. Briefly, the CD31-postive or Endomucin-positive (red) area relative to the total BM area (visualized in blue) was calculated using Image J software (http://rsbweb,nih,gov/ij/).

For whole-mount immunostaining, retinas were collected from adult mice after systemic or local SLIT3 administration in bone fracture models. Immunofluorescence staining was performed as described previously[42]. The mice were intra-orbitally injected with anti-VE-cadherin Ab (clone BV13, Biolegend).

For histological analysis, hindlimbs were dissected from the mice or human callus, fixed in 10% neutral buffered formalin for 24–48 hours, and decalcified by daily changes of 15% tetrasodium EDTA for 2 weeks. Tissues were dehydrated by passage through an ethanol series, cleared twice in xylene, embedded in paraffin, and sectioned at 7μm thickness. Decalcified sections were stained with hematoxylin and eosin (H&E). We incubated the slides with primary antibody to mouse EMCN (sc-65495, Santa Cruz, 1:200) and human Slit3 (ab198726, Abcam 1:50) at 37 °C for 2 h and subsequently used a horseradish peroxidase–streptavidin detection system (Dako) to detect the immunoreactivity. We measured the number and volume of positively stained vessels in four random visual fields of callus in 3 sequential sections per mouse in each group.

For histomorphometry, mice were injected with calcein (25mg/kg, Sigma), and undecalcified sections of the lumbar vertebrae were stained using von Kossa and TRAP as previously described[29]. Static and dynamic histomorphometric analysis was performed with using the Osteomeasure Analysis System (Osteometrics) following standard nomenclature as previously described[43]. Bone volume/total volume (BV/TV), bone formation rate/bone surface (BFR/BS, $\mu m^3 \, \mu m^{-1} \, yr^{-1}$), mineral apposition rate (MM, um Day^{-1}), osteoblast surface/bone surface (Ob.S/BS, %) and osteoclast number/bone perimeter (No. OC/Bpm) were analyzed.

Flow cytometry and Cell Sorting

Femur and tibia were dissected from mutant mice and control groups after removing surrounding connective tissues. The metaphysis region and diaphysis regions of bone was crushed in Hanks Balanced Salt Solution (Life Technologies) containing 10 mM HEPES (pH 7.2) (CellGro) and enzymatically digested with 2.5 mg/mL Collagenase A (Roche) and 1 unit/mL Dispase II (Roche) for 15 minutes at 37°C under gentle agitation. The resulting cell suspensions were filtered (40 μm), washed using PBS (pH 7.2) containing 0.5% BSA (Fraction V) and 2 mM EDTA. After washing, equal numbers of cells per mouse were blocked with Purified Rat Anti-Mouse CD16/CD32 (BD Biosciences) for 30 min on ice, then stained with APC-conjugated EMCN antibody (ebioscience 50-5851-80), PE-conjugated CD31 (ebioscience 12-0311-81), FITC-conjugated CD45 (Tonbo 35-0451), APC/Cy7-conjugated Ter119 (Biolegend 116223) and PerCP-Cy5.5-conjugated CD146 (BD Biosciences 562231) for 45 min on ice. After washing, cells were resuspended in PBS (pH 7.2) with 2 mM EDTA and 1μg/mL 4–6, Diamidino-2-Phenylindole (DAPI) (live/dead exclusion) for analysis on an LSRII flow cytometer system (BD Biosciences) cytometer and analyzed using FlowJo software (TreeStar). Cell sorting was performed with a FACS Aria II SORP cell sorter (Becton Dickinson) at Weill Cornell Medical College, with exclusion of DAPI$^+$ cells and doublets. The strategy to sort CD31^{hi}EMCN^{hi} endothelial cells is diagrammed in extended figure 1-c.

Osteoblast Culture and Differentiation Assays

Primary calvarial osteoblasts were isolated from 5 day-old mice by triple collagenase/dispase II digestion. Cells were cultured in α-MEM medium (Gibco) containing 10% FBS, 2 mM L-glutamine, 1% penicillin/streptomycin, 1% Hepes, and 1% nonessential amino acids and differentiated with ascorbic acid and β-glycerophosphate. Conditioned medium was collected from culture of primary osteoblasts and stocked at −80 °C. hMSCs were cultured and differentiated into osteoblasts using a commercial kit (Cyagen). All cells were routinely tested to be mycoplasma negative.

For staining of extracellular matrix mineralization, cells were fixed with 10% neutral buffered formalin and stained with alizarin red. Mineralization activity was measured by colorimetric analysis. For alkaline phosphatase (ALP) activity, osteoblasts were fixed with 10% neutral formalin buffer and stained with the solution containing Fast Blue and Naphthol (Sigma-Aldrich). Alternatively, osteoblasts were incubated with 10-fold diluted Alamar Blue solution, washed, and incubated with a solution containing 6.5 mM Na_2CO_3, 18.5 mM $NaHCO_3$, 2 mM $MgCl_2$, and phosphatase substrate (Sigma-Aldrich). ALP activity was measured by a sepectrophotometer (Thermo).

Osteoclast Culture and Differentiation

Murine BM cells were flushed from the femur and tibia of mice and cultured in petri dishes in α-MEM medium with 10% FBS and 20ng/ml of rM-CSF. Nonadherent cells were replated into tissue culture dishes and cultured in the same medium for 3 d to obtain osteoclast precursors. The osteoclast precursors then differentiated into osteoclasts in the presence of human RAMKL (50 ng/ml; PeproTech) and M-CSF for 3 days. Peripheral blood mononuclear cells from the whole blood of healthy volunteers were isolated by density gradient centrifugation using Ficoll (Invitrogen, Carlsbad, CA). CD14-positive cells were purified from fresh PBMCs using anti-CD14 magnetic beads (Miltenyi Biotec, Auburn, CA), as recommended by the manufacturer. Human monocytes were cultured in a-MEM with 10% FBS in the presence of M-CSF (20 ng/ml; PeproTech, Rocky Hill, NJ) for 2 d to obtain monocyte-derived macrophages. Experiments with human cells were approved by the Hospital for Special Surgery Institutional Review Board.

Endothelial cell culture and functional assays

Mouse BM derived late-stage endothelial progenitor outgrowth cells (EPOCs) were obtained from BioChain (7030031) and cultured in growth medium (BioChain Z7030035) as described previously[3]. Endothelial cell migration assay was set up in Transwell-24 well plates with 8-um pore filters. Briefly, 1×10^5 cells/well after 1h serum starvation were seeded in the upper chamber, then incubated with conditioned medium from osteoblasts and control in the lower chambers for a further 3h. The cells in the upper surface of each filter were removed with cotton swabs. The cells that migrated into the lower surface were fixed with 4% PFA for 30 min and then stained with crystal violet. The cell numbers were quantified by counting a centered microscope field per each filter (5 wells for each condition). Endothelial cell wound healing assays were conducted in 12-well plates precoated with gelatin (Stemcell Technologies). 3×10^5 cells/well were plated overnight and stimulated with a wound in the form of a single linear scratch made with a yellow pipette tip. After gently

washing the well twice, cells were cultured in medium with SLIT3 or vehicle. At 6 and 12 hours after injury, cells were stained by 0.5% crystal violet and photographed. The width of the wound area was quantitatively evaluated using ImageJ (http://rsb.info.nih.gov/ij/download.html). Endothelial cell proliferation assays were conducted in 96-well plates pre-coated with gelatin (Stemcell Technologies). EPOCs (3×10^4 cells/well) were seeded in the medium with a serial dilution of SLIT3 protein or vehicle in plates. At 0, 24, 48 hours after seeding, cells were incubated with 10-fold diluted Alamar Blue solution (Thermo Fisher) and the supernatant was evaluated with a sepectrophotometer (Thermo) (5 wells for each condition). Endothelial cell tube formation assay was conducted in 96-well plates pre-coated with Matrigel (BD). After 1h serum starvation, EPOCs (3×10^4 cells/well) were seeded in conditioned medium dilution or control medium on polymerized Matrigel in plates. After 5h incubation at 37 °C, the number of tube branches each well was observed and quantified by counting four random fields per well with microscopy (5 wells for each condition).

Quantitative real-time PCR analysis

Total RNA was extracted using TRIzol reagent (Invitrogen) or RNeasy Mini Kit (Qiagen), and reverse transcription was performed with the High-Capacity cDNA Reverse Transcription Kit from Applied Biosystems according to the manufacturer's instructions. We performed quantitative analysis of gene expression using SYBR® Green PCR Master Mix (Applied Biosystems) with the Mx3000P real-time PCR system (Agilent Technologies). *Hprt* expression was used as an internal control. The primers used for PCR are described in the Supplementary Table 1.

RNA sequencing and analysis

Reads were aligned to the mm9 mouse transcripts using STAR(version 2.3.0e)[44] using default parameters and resulting bam files were sorted and indexed using samtools. Gene counts were obtained by applying feature counts (version 1.4.3)[45] to sorted bam files, and only unique-mapping reads were used. Genes without any expression counts in any sample were discarded. The DESeq2 (version 1.4.5) R package[46] was employed to normalize gene count data, and then detect differentially expressed genes (DEG) between mutant mice and control groups with (FDR<0.1 and absolute log2 fold-change>0.5). Mosaic version 1.1 was used to retrieve gene ontology (GO) information for all genes of the mouse genome[47]. Functional analysis was performed on DEG with DAVID[48] (version 6.7) and biological process GO terms with enrichment $p<0.05$ were selected as overrepresented functions.

Western blot analysis

Western blot analysis was performed according to a previously described standard protocol. [49] Primary antibodies were specific for SLIT3 (1:500; R&D Systems, AF3629), ROBO1 (1:500; Abcam, ab7279), ROBO2 (1:1000; Abcam, ab75014), YAP (1:1,000; Cell Signaling, 4912), p-YAP (1:1,000; Cell signaling, 4911), AKT (1:1,000; Cell Signaling, 4691), p-AKT (1:1,000; Cell Signaling, 4060), ERK (1:1,000; Cell Signaling, 9102), p-ERK (1:1,000; Cell Signaling, 9101) and beta-actin (1:5,000; sc-47778, Santa Cruz) or Hsp90 (1:1000; sc-13119, Santa Cruz). Secondary anti-mouse/rabbit HRP-conjugated antibodies were subsequently applied.

ELISA analysis

SLIT3 ELISA (Lifespan LS-F7173) and CTX ELISA (Lifespan LS-F21349) analysis was performed by using a kit. All ELISA assays were run according to the manufacturer's instructions.

Bone fracture model

All surgical procedures were performed under isoflurane (1–4%) anesthesia via nosecone. Surgical sites were sterilized using a betadine/iodide/isopropanol prep after hair removal by a clipper with a #40 blade and depilatory cream (Nair). After surgery, the visceral lining or muscle was sutured with absorbable Ethicon vicryl sutures (VWR, Cat #95057-014) prior to closing the skin with wound clips that were then removed 2 weeks post-operatively. Animals received intraperitoneal Buprenex (0.5 mg/kg) and oral Meloxicam (2.0 mg/kg) as analgesia prior to surgery and once every 24 hours post-surgery for 3 days. All surgical procedures are approved by the IACUC of Weill Cornell Medical College (Protocol #2012-0005).

Bone fracture was done following previously described protocols with modifications[50]. In brief, after anesthesia and surgical site sterilization, an incision above the right anterolateral femur was made. The femur and patella were then exposed and a 27-gauge syringe needle was inserted parallel with the long axis of the femur through the patellar groove into the marrow cavity. The needle was then removed and a single cut was made in the middle of the femoral diaphysis using a dremel saw with a diamond thin cutting wheel (VWR, Cat#100230-724). A blunt 25 gauge needle was then inserted into the marrow space through the hole made in the patella to stabilize the fracture. The needle was then trimmed to avoid it from projecting into the patella-femoral joint space. Muscle was then placed over the osteotomy site and stitched with absorbable sutures prior to closing the skin with wound clips.

When assessing the therapeutic effects of SLIT3, 1mg/kg body weight of SLIT3 recombinant protein (R&D) or vehicle was intravenous injected to the mice twice per week for 3 weeks after the surgery. Alternatively, the gelatin sponge was manually soaked with SLIT3 (300ug/ml in PBS) or vehicle for 1 hour on ice and immediately placed to the surgical fracture area. All animals were euthanized by CO_2 at time points indicated.

Ovariectomy-induced bone loss

For the prophylactic model, 12-week-old female mice (JAX) were anesthetized and bilaterally ovariectomized or sham operated. Ovariectomized mice were given twice weekly intravenous injections of 1mg per kg body weight of SLIT3 or vehicle or daily sc injections of 80ug/kg PTH (1–34) for 6 weeks starting 2 weeks after ovariectomy. For the model where SLIT3 was delivered in a therapeutic manner after osteopenia onset, OVX was performed in 12 week old mice, mice were observed for 8 weeks post-OVX to allow for onset of osteopenia, and then mice were treated with SLIT3 (1mg/kg) or vehicle for 6 further weeks. All mice were then randomly assigned to one of four groups: Sham, OVX +vehicle, OVX + SLIT3 and OVX + PTH. Three days after the last injection, all of the mice were euthanized and subjected to bone analysis as described earlier.

Biomechanical Analysis

All bones were tested to failure using four-point bending on a precision electromagnetic-based load frame (EnduraTEC ELF 3200, Bose Corporation, Minnetonka, MC). Femurs were placed with the posterior surface on the lower supports, spaced 9.9 mm apart. The upper supports were spaced 3.3 mm. Load was applied at a rate of 0.1 mm/s until failure occurred. The failure load (N) and bending stiffness (N/mm^2) within the elastic range were calculated from the force-displacement curves and the four-point dimensions.

Human bone callus collection

The project was approved by the Ethics Committee of Shaoxing People's Hospital (No. 080) and the protocol was carried out in accordance with approved guidelines. Preoperative informed consent was obtained from each patient. From January 2010 to June 2014, bone callus samples were obtained from patients undergoing surgical treatment in the Department of Orthopedics of Shaoxing People's Hospital. Callus was collected from patients who required surgical treatment for failure of skeletal traction. Inclusion criteria were as follows: (1) surgeries after failure of conservative treatment or external fixation were applied temporarily before open reduction and plate fixation for long bone fractures; (2) secondary surgeries after failure of internal fixation, including loosened or broken plates or screws, bent or broken intramedullary nails, and fracture angulation and aversion abnormalities; and (3) secondary surgeries for hypertrophic nonunion. Exclusion criteria were as follows: (1) fracture complicated with microbial infection; (2) fracture complicated with brain injury; (3) bone tumors; (4) systemic bone-related diseases; and (5) patients treated with hormones, steroids, vitamin D, or calcium. Further demographic information is published[51].

Statistical Methods

All data were presented as the mean ± s.e.m. Sample sizes were calculated on the assumption that a 30% difference in the parameters measured would be considered biologically significant with an estimate of sigma of 10–20% of the expected mean. Alpha and Beta were set to the standard values of .05 and 0.8, respectively. No animals or samples were excluded from analysis, and, where applicable, animals were randomized to treatment versus control groups. Statistical methods are indicated in figure legends. The GraphPad PRISM software (v6.0a, La Jolla, CA) was used for statistical analysis. $P < 0.05$ was considered statistically significant. $*P<0.05$, $**P<0.01$, $***P<0.001$.

Supplementary Material

Refer to Web version on PubMed Central for supplementary material.

Acknowledgments

References

1. Kusumbe AP, Ramasamy SK, Adams RH. Coupling of angiogenesis and osteogenesis by a specific vessel subtype in bone. Nature. 2014; 507:323–328. [PubMed: 24646994]

2. Ramasamy SK, Kusumbe AP, Wang L, Adams RH. Endothelial Notch activity promotes angiogenesis and osteogenesis in bone. Nature. 2014; 507:376–380. [PubMed: 24647000]

3. Xie H, et al. PDGF-BB secreted by preosteoclasts induces angiogenesis during coupling with osteogenesis. Nat Med. 2014; 20:1270–1278. [PubMed: 25282358]

4. Shim JH, et al. Schnurri-3 regulates ERK downstream of WNT signaling in osteoblasts. J Clin Invest. 2013; 123:4010–4022. [PubMed: 23945236]

5. Jones DC, et al. Regulation of adult bone mass by the zinc finger adapter protein Schnurri-3. Science. 2006; 312:1223–1227. [PubMed: 16728642]

6. Nguyen Ba-Charvet KT, et al. Slit2-Mediated chemorepulsion and collapse of developing forebrain axons. Neuron. 1999; 22:463–473. [PubMed: 10197527]

7. Jaworski A, Tessier-Lavigne M. Autocrine/juxtaparacrine regulation of axon fasciculation by Slit-Robo signaling. Nat Neurosci. 2012; 15:367–369. [PubMed: 22306607]

8. Jones CA, et al. Robo4 stabilizes the vascular network by inhibiting pathologic angiogenesis and endothelial hyperpermeability. Nat Med. 2008; 14:448–453. [PubMed: 18345009]

9. Rama N, et al. Slit2 signaling through Robo1 and Robo2 is required for retinal neovascularization. Nat Med. 2015; 21:483–491. [PubMed: 25894826]

10. Vasam G, et al. Reversal of Bone Marrow Mobilopathy and Enhanced Vascular Repair by Angiotensin-(1-7) in Diabetes. Diabetes. 2017; 66:505–518. [PubMed: 27856608]

11. Geutskens SB, et al. Control of human hematopoietic stem/progenitor cell migration by the extracellular matrix protein Slit3. Lab Invest. 2012; 92:1129–1139. [PubMed: 22614124]

12. Zhou WJ, Geng ZH, Spence JR, Geng JG. Induction of intestinal stem cells by R-spondin 1 and Slit2 augments chemoradioprotection. Nature. 2013; 501:107–111. [PubMed: 23903657]

13. Mehlen P, Delloye-Bourgeois C, Chedotal A. Novel roles for Slits and netrins: axon guidance cues as anticancer targets? Nat Rev Cancer. 2011; 11:188–197. [PubMed: 21326323]

14. Zhang B, et al. Repulsive axon guidance molecule Slit3 is a novel angiogenic factor. Blood. 2009; 114:4300–4309. [PubMed: 19741192]

15. Paul JD, et al. SLIT3-ROBO4 activation promotes vascular network formation in human engineered tissue and angiogenesis in vivo. J Mol Cell Cardiol. 2013; 64:124–131. [PubMed: 24090675]

16. Zhang J, Link DC. Targeting of Mesenchymal Stromal Cells by Cre-Recombinase Transgenes Commonly Used to Target Osteoblast Lineage Cells. J Bone Miner Res. 2016; 31:2001–2007. [PubMed: 27237054]

17. Chen J, et al. Osx-Cre targets multiple cell types besides osteoblast lineage in postnatal mice. PLoS One. 2014; 9:e85161. [PubMed: 24454809]

18. Su AI, et al. A gene atlas of the mouse and human protein-encoding transcriptomes. Proc Natl Acad Sci U S A. 2004; 101:6062–6067. [PubMed: 15075390]

19. Yuan W, et al. A genetic model for a central (septum transversum) congenital diaphragmatic hernia in mice lacking Slit3. Proc Natl Acad Sci U S A. 2003; 100:5217–5222. [PubMed: 12702769]

20. Geutskens SB, Hordijk PL, van Hennik PB. The chemorepellent Slit3 promotes monocyte migration. J Immunol. 2010; 185:7691–7698. [PubMed: 21078908]

21. Naska S, Lin DC, Miller FD, Kaplan DR. p75NTR is an obligate signaling receptor required for cues that cause sympathetic neuron growth cone collapse. Mol Cell Neurosci. 2010; 45:108–120. [PubMed: 20584617]

22. Howitt JA, Clout NJ, Hohenester E. Binding site for Robo receptors revealed by dissection of the leucine-rich repeat region of Slit. EMBO J. 2004; 23:4406–4412. [PubMed: 15496984]

23. Liu Z, et al. Extracellular Ig domains 1 and 2 of Robo are important for ligand (Slit) binding. Mol Cell Neurosci. 2004; 26:232–240. [PubMed: 15207848]

24. Shin M, et al. Vegfa signals through ERK to promote angiogenesis, but not artery differentiation. Development. 2016; 143:3796–3805. [PubMed: 27578780]

25. Choi HJ, et al. Yes-associated protein regulates endothelial cell contact-mediated expression of angiopoietin-2. Nat Commun. 2015; 6:6943. [PubMed: 25962877]

26. Blockus H, Chedotal A. Slit-Robo signaling. Development. 2016; 143:3037–3044. [PubMed: 27578174]

27. Sakabe M, et al. YAP/TAZ-CDC42 signaling regulates vascular tip cell migration. Proc Natl Acad Sci U S A. 2017; 114:10918–10923. [PubMed: 28973878]

28. Bouxsein ML, et al. Ovariectomy-induced bone loss varies among inbred strains of mice. J Bone Miner Res. 2005; 20:1085–1092. [PubMed: 15940361]

29. Fukuda T, et al. Sema3A regulates bone-mass accrual through sensory innervations. Nature. 2013; 497:490–493. [PubMed: 23644455]

30. Zhang Y, et al. Implant-derived magnesium induces local neuronal production of CGRP to improve bone-fracture healing in rats. Nat Med. 2016; 22:1160–1169. [PubMed: 27571347]

31. Xu R. Semaphorin 3A: A new player in bone remodeling. Cell Adh Migr. 2014; 8:5–10. [PubMed: 24589620]

32. Ramalingam P, Poulos MG, Butler JM. Regulation of the hematopoietic stem cell lifecycle by the endothelial niche. Curr Opin Hematol. 2017; 24:289–299. [PubMed: 28594660]

33. Buza JA 3rd, Einhorn T. Bone healing in 2016. Clin Cases Miner Bone Metab. 2016; 13:101–105. [PubMed: 27920804]

34. Sun H, Dai K, Tang T, Zhang X. Regulation of osteoblast differentiation by slit2 in osteoblastic cells. Cells Tissues Organs. 2009; 190:69–80. [PubMed: 19033678]

35. Leder BZ, et al. Denosumab and teriparatide transitions in postmenopausal osteoporosis (the DATA-Switch study): extension of a randomised controlled trial. Lancet. 2015; 386:1147–1155. [PubMed: 26144908]

36. Wein MN, et al. Control of bone resorption in mice by Schnurri-3. Proc Natl Acad Sci U S A. 2012; 109:8173–8178. [PubMed: 22573816]

37. Chen MJ, Yokomizo T, Zeigler BM, Dzierzak E, Speck NA. Runx1 is required for the endothelial to haematopoietic cell transition but not thereafter. Nature. 2009; 457:887–891. [PubMed: 19129762]

38. Rodda SJ, McMahon AP. Distinct roles for Hedgehog and canonical Wnt signaling in specification, differentiation and maintenance of osteoblast progenitors. Development. 2006; 133:3231–3244. [PubMed: 16854976]

39. Lu Y, et al. DMP1-targeted Cre expression in odontoblasts and osteocytes. J Dent Res. 2007; 86:320–325. [PubMed: 17384025]

40. Park D, et al. Endogenous bone marrow MSCs are dynamic, fate-restricted participants in bone maintenance and regeneration. Cell Stem Cell. 2012; 10:259–272. [PubMed: 22385654]

41. Xu R, et al. c-Jun N-Terminal Kinases (JNKs) Are Critical Mediators of Osteoblast Activity In Vivo. J Bone Miner Res. 2017; 32:1811–1815. [PubMed: 28561373]

42. Tual-Chalot S, Allinson KR, Fruttiger M, Arthur HM. Whole mount immunofluorescent staining of the neonatal mouse retina to investigate angiogenesis in vivo. J Vis Exp. 2013:e50546. [PubMed: 23892721]

43. Dempster DW, et al. Standardized nomenclature, symbols, and units for bone histomorphometry: a 2012 update of the report of the ASBMR Histomorphometry Nomenclature Committee. J Bone Miner Res. 2013; 28:2–17. [PubMed: 23197339]

44. Dobin A, et al. STAR: ultrafast universal RNA-seq aligner. Bioinformatics. 2013; 29:15–21. [PubMed: 23104886]

45. Liao Y, Smyth GK, Shi W. featureCounts: an efficient general purpose program for assigning sequence reads to genomic features. Bioinformatics. 2014; 30:923–930. [PubMed: 24227677]

46. Love MI, Huber W, Anders S. Moderated estimation of fold change and dispersion for RNA-seq data with DESeq2. Genome Biol. 2014; 15:550. [PubMed: 25516281]

47. Zhang C, et al. Mosaic: making biological sense of complex networks. Bioinformatics. 2012; 28:1943–1944. [PubMed: 22576176]

48. Huang da W, Sherman BT, Lempicki RA. Systematic and integrative analysis of large gene lists using DAVID bioinformatics resources. Nat Protoc. 2009; 4:44–57. [PubMed: 19131956]

49. Greenblatt MB, et al. MEKK2 mediates an alternative beta-catenin pathway that promotes bone formation. Proceedings of the National Academy of Sciences of the United States of America. 2016; 113:E1226–1235. [PubMed: 26884171]

50. Bradaschia-Correa V, et al. The Selective Serotonin Reuptake Inhibitor Fluoxetine Directly Inhibits Osteoblast Differentiation and Mineralization During Fracture Healing in Mice. J Bone Miner Res. 2017; 32:821–833. [PubMed: 27869327]

51. Han W, et al. The osteogenic potential of human bone callus. Sci Rep. 2016; 6:36330. [PubMed: 27796345]
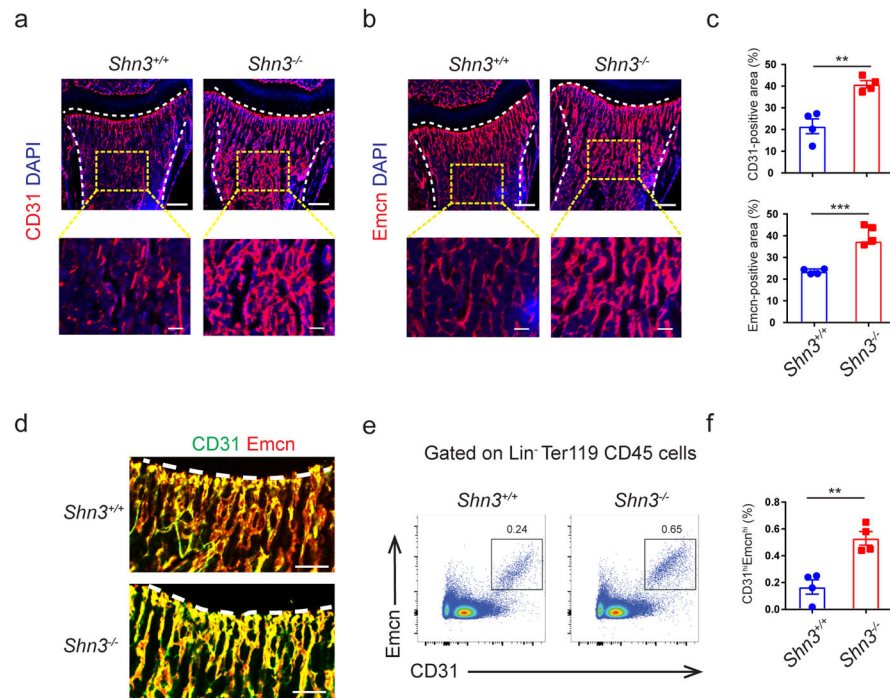
Figure 1.

Shn3^{−/−} mice have higher levels of CD31^{hi}EMCN^{hi} endothelium. (**a**, **b**) Representative confocal images ($n = 4$ total images per group) of 2-week-old *Shn3*^{+/+} and *Shn3*^{−/−} male mouse femurs stained with CD31 (**a**) or Endomucin (EMCN) (**b**) (red) and 4′,6-diamidino-2-phenylindole (DAPI, blue). Growth plate and cortical bone are marked with a dashed line. Scale bars, 300μm (top) and 50μm (bottom). (**c**) Quantification of relative CD31-postive (top) and EMCN-positive vessel area (bottom) in the bone marrow (BM) cavity of the femur sections in 2-week-old *Shn3*^{+/+} and *Shn3*^{−/−} male mice ($n = 4$ per group). (**d**) Representative images ($n = 3$ total images per group) of CD31 (green) and EMCN (red) dual immunostained femur sections from the femur in 2-week-old male mice. The growth plate is marked. Scale bars, 100μm. (**e**, **f**) Representative flow cytometry plots (**e**) with quantification (**f**) of CD31^{hi}EMCN^{hi} endothelial cells from the femurs of 2-week-old *Shn3*^{+/+} and *Shn3*^{−/−} mice ($n = 4$ per group). Values represent mean ± s.e.m.; **$P < 0.01$, ***$P < 0.001$ by an unpaired two-tailed Student's *t*-test in all panels.
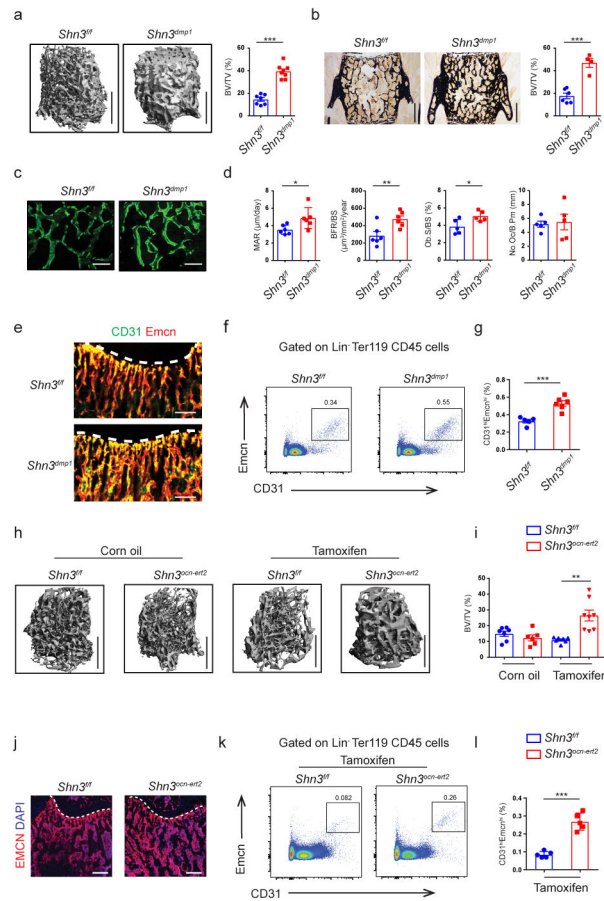
Figure 2.
Ablation of *Shn3* in osteoblasts enhances osteogenesis and angiogenesis in vivo. (**a**)
Representative μCT images of the trabecular bone in the distal femur (left) and bone
volume/total volume (BV/TV) (right) in *Shn3*[f/f] (*n* = 7) and *Shn3*[dmp1] (*n* = 8) male mice at
8-weeks of age. Scale bars, 1mm. (**b**) Representative histomorphometric images of the L3
vertebrae (left) and BV/TV (right) in *Shn3*[f/f] (*n* = 6) and *Shn3*[dmp1] (*n* = 4) male mice at 8-
weeks of age. Scale bars, 500μm. (**c, d**) Representative images of calcein double labeling (**c**)
and quantification of histomorphometric parameters (**d**) of the L3 vertebrae in *Shn3*[f/f] and
Shn3[dmp1] male mice at 8-week of age. Trabecular mineral apposition rate (MAR, mm day
$^{-1}$), bone formation rate/bone surface (BFR/BS, mm^3 mm^{-2} yr^{-1}), osteoclast number/bone
perimeter (No. Oc./B. Pm) and osteoblast surface/bone surface (Ob.S/BS, %). Scale bars,
300μm. MAR and BFR/BS: *n* = 6 per group; No. Oc./B. Pm and Ob.S/BS: *n* = 5 per group.
(**e**) Representative confocal images (*n* = 3 total images per group) of femur sections from 2-
week old *Shn3*[f/f] and *Shn3*[dmp1] male mice with EMCN (red) and CD31 (green). Growth
plate is marked with a dashed line. Scale bars, 100 μm. (**f, g**) Representative flow cytometry
plots (**f**) and relative frequency of CD31^{hi}EMCN^{hi} endothelial cells (**g**) from the femurs of
2-week-old male *Shn3*[dmp1] (*n* = 6) and *Shn3*[f/f] (*n* = 5) mice. (**h, i**) Representative μCT
images of the trabecular bone in the distal femur metaphysis (**h**) and relative quantitative
analysis of BV/TV (**i**) in *Shn3*[f/f] (oil =7; tamoxifen =7) and *Shn3*[ocn-ert2] male mice (oil =6;
tamoxifen =8). Analysis was performed 12-weeks after tamoxifen injection into 4-week old

mice. Scale bars, 1mm. (**j**) Representative confocal images (n = 3 total images per group) of EMCN (red) and DAPI (blue) immunostained femur sections from *Shn3*$^{f/f}$ and *Shn3*$^{ocn-ert2}$ male mice at 4-weeks after tamoxifen injection into 4-week old mice. Growth plate is marked with a dashed line. Scale bars, 300 μm. (**k**, **l**) Representative flow cytometry plots (**k**) and relative frequency of CD31^{hi}EMCN^{hi} endothelial cells (**l**) from the femurs of *Shn3*$^{f/f}$ and *Shn3*$^{ocn-ert2}$ male mice (n = 5 per group), 6-weeks after tamoxifen injection into 4-weeks old mice. Values represent mean ± s.e.m.; *$P < 0.05$, **$P < 0.01$, ***$P < 0.001$ all by an unpaired two-tailed Student's *t*-test or by one-way ANOVA followed by a Dunnett's test in all panels.
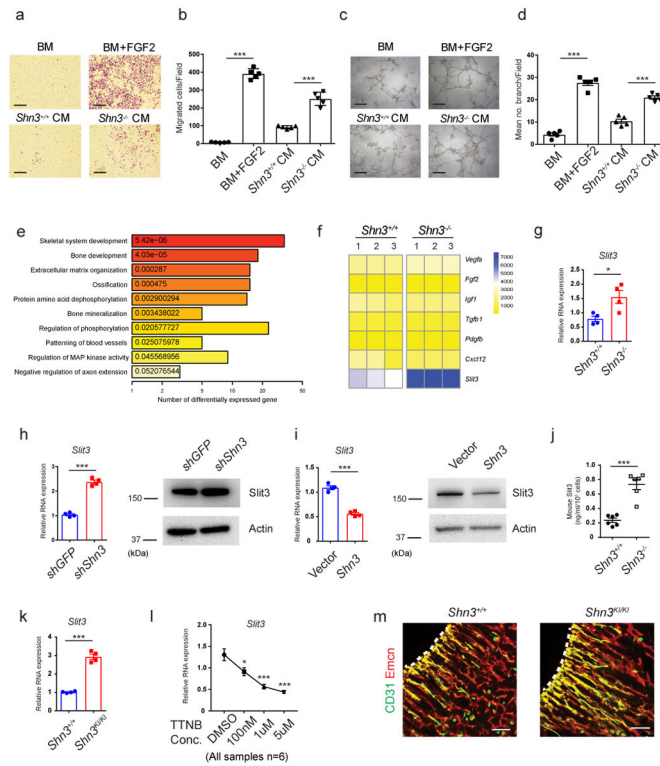
Figure 3.

Inhibition of *Shn3* enhances *Slit3* expression in osteoblasts. (**a**, **b**) Representative images (**a**) and relative quantification (**b**) of a transwell migration assay of BM-derived endothelial progenitor outgrowth cells (EPOCs). Basal medium, (BM); Conditioned medium, (CM). *n* = 5 per group. (**c**, **d**) Representative images (**c**) and relative quantification of tube branch numbers (**d**) of a Matrigel tube formation assay with EPOCs. *n* = 5 per group. (**e**) Gene ontology (GO) enrichment analysis of genes differentially expressed in *Shn3*$^{−/−}$ osteoblasts relative to *Shn3*$^{+/+}$ osteoblasts (**f**) Proangiogenic gene expression in primary *Shn3*$^{+/+}$ and *Shn3*$^{−/−}$ osteoblasts. (**g**) Real-time PCR of *Slit3* expression in *Shn3*$^{+/+}$ and *Shn3*$^{−/−}$ osteoblasts. *n* = 4 per group. (**h**) Messenger RNA (mRNA) (left) and protein (right) levels of *Slit3* in human mesenchymal stromal cells (hMSCs) expressing a GFP targeting control or *Shn3* shRNAs cultured under osteogenic conditions. *n* = 4 per group. (**i**) mRNA (left) and protein (right) levels of *Slit3* in hMSCs overexpressing a vector control or *Shn3* cultured under osteogenic conditions.. *n* = 4 per group. (**j**) ELISA for SLIT3 secretion by *Shn3*$^{+/+}$ and *Shn3*$^{−/−}$ osteoblasts. *n* = 6 per group. (**k**) Real-time PCR analysis of *Slit3* in *Shn3*$^{+/+}$ and *Shn3*$^{KI/KI}$ osteoblasts (*n* = 4). (**l**) Real-time PCR analysis of *Slit3* in hMSCs treated with trametinib (TTNB). *n* = 6 per group. (**m**) Representative confocal images (*n* = 3 total images per group) of CD31 (green) and EMCN (red) immunostained sections from the femurs of 2-week-old *Shn3*$^{+/+}$ and *Shn3*$^{KI/KI}$ male mice. Growth plate is marked with a dashed line. Scale bars, 100μm. Values represent mean ± s.e.m.; *P < 0.05, **P < 0.01, ***P < 0.001 by an unpaired two-tailed Student's *t*-test or one-way ANOVA followed by a Dunnett's test in all panels. All immunoblots are cropped from the original.
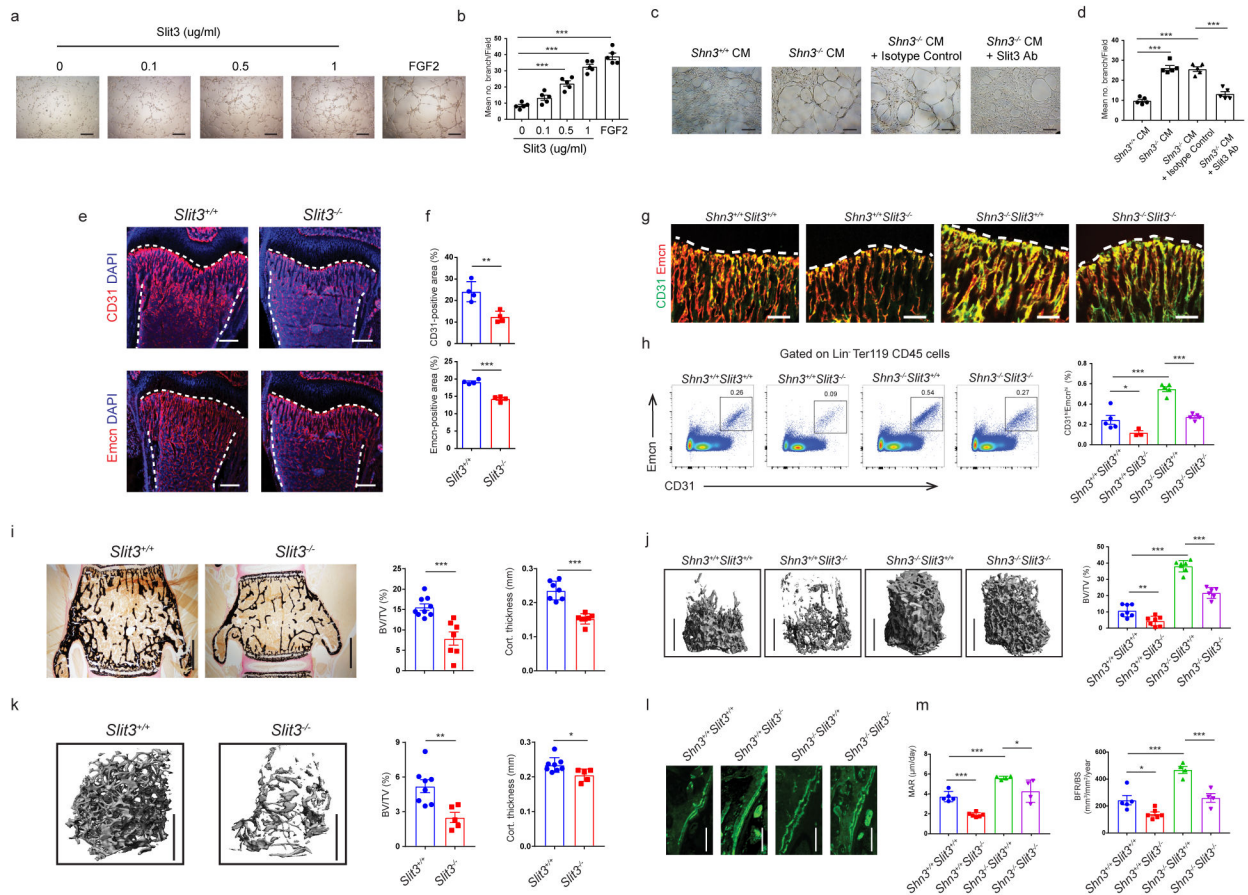
Figure 4.

Slit3⁻/⁻ mice have reduced skeletal vasculature and bone mass *in vivo*. (**a–d**) Representative images (**a**, **c**) and relative quantification of tube branch numbers (**b**, **d**) in a Matrigel tube formation assay with EPOCs. $n = 5$ per group. Scale bars, 200μm. (**c**, **d**) Where indicated, a SLIT3-neutralizing antibody or isotype control was added. Scale bars, 200μm. (**e**, **f**) Representative confocal images of CD31 or EMCN (red) and DAPI (blue) immunostained sections (**e**) and relative quantification (**f**) of CD31-postive or EMCN-positive vessel area in the BM cavity of the femurs from male *Slit3⁺/⁺* and *Slit3⁻/⁻* mice at 2-weeks of age. $n = 4$ per group. Growth plate and cortical bone are marked with a dashed line. Scale bars, 300μm. (**g**, **h**) Representative confocal images ($n = 3$ total images per group) of CD31 (green) and EMCN (red) immunostained bone sections (**g**) flow cytometry dot plots (**h**, left), and relative frequency of CD31^hiEMCN^hi endothelial cells (**h**, right) of the femur in 2 week-old *Shn3⁺/⁺ Slit3⁺/⁺* ($n = 5$), *Shn3⁺/⁺ Slit3⁻/⁻* ($n = 3$), *Shn3⁻/⁻ Slit3⁺/⁺* ($n = 5$) and *Shn3⁻/⁻ Slit3⁻/⁻* mice ($n = 5$). Growth plate is marked with a dashed line. Scale bars, 100μm. (**i**) Representative histological images (left) and relative BV/TV (middle) of the L3 vertebrae (*Slit3⁺/⁺* = 9, *Slit3⁻/⁻* = 7) and cortical thickness (right) of distal femoral metaphyseal regions (*Slit3⁺/⁺* = 7, *Slit3⁻/⁻* = 6) at 6-weeks of age. Scale bars, 500μm. (**j**) Representative μCT images of the trabecular bone in the distal femur metaphysis (left) and relative BV/TV analysis of 6 week-old *Shn3⁺/⁺ Slit3⁺/⁺*($n = 7$), *Shn3⁺/⁺ Slit3⁻/⁻*($n = 7$), *Shn3⁻/⁻ Slit3⁺/⁺*($n = 7$) and *Shn3⁻/⁻ Slit3⁻/⁻* mice ($n = 6$) (right). Scale bar, 1mm. (**k**) Representative μCT images of the

trabecular bone in the distal femur metaphysis (left) and relative trabecular BV/TV analysis (middle) and cortical bone thickness in the femoral midshaft from male $Slit3^{+/+}$ mice ($n = 8$) and $Slit3^{-/-}$ mice ($n = 5$) at 12-weeks of age. Scale bars, 1mm. (**l, m**) Representative images of calcein labelling (**I**) and relative histomorphometric quantification of MAR and BFR/BS in 6 week-old $Shn3^{+/+} Slit3^{+/+}$($n = 5$), $Shn3^{+/+} Slit3^{-/-}$($n = 6$), $Shn3^{-/-} Slit3^{+/+}$($n = 4$) and $Shn3^{-/-} Slit3^{-/-}$ male mice ($n = 4$). Scale bars, 100μm. Values represent mean ± s.e.m.; *$P <$ 0.05, **$P < 0.01$ and ***$P < 0.001$ by an unpaired two-tailed Student's t-test or one-way ANOVA followed by a Dunnett's test in all panels.
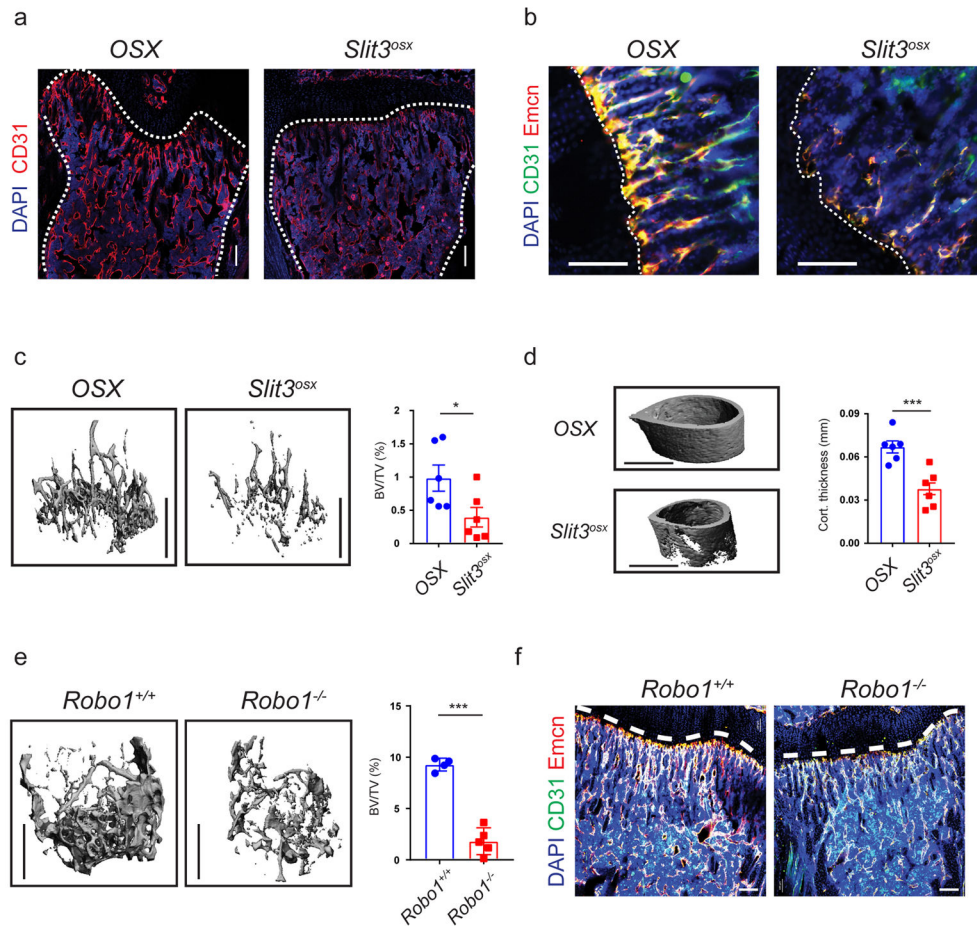
Figure 5.
Osteoblast derived *Slit3* controls osteogenesis and CD31^{hi}EMCN^{hi} endothelium via ROBO1. (**a**, **b**) Representative confocal images ($n = 3$ total images per group) of CD31 (red) and DAPI (blue) (**a**) or CD31 (green), EMCN (red) and DAPI (blue) (**b**) stained femur sections in 2 week-old *OSX Cre* and *Slit3^{osx}* male mice. Growth plate and cortical bone are marked with a dashed line. Scale bars, 100μm. (**c**) Representative μCT images of the trabecular bone in the distal femur metaphysis (left) and relative BV/TV analysis (right) of 3 week-old *OSX Cre* and *Slit3^{osx}* male mice. Scale bar, 1mm. $n = 6$ per group. (**d**) Representative μCT images of the femoral midshaft (left) and relative cortical bone thickness analysis (right) of 3 week-old *OSX Cre* and *Slit3^{osx}* male mice. Scale bar, 1mm. $n = 6$ per group. (**e**) Representative μCT images of the trabecular bone in the distal femur metaphysis (left) and relative BV/TV analysis in 12 week-old *Robo1$^{+/+}$* ($n = 4$) and *Robo1$^{-/-}$* female mice ($n = 5$). Scale bars, 1mm. (**f**) Representative confocal images ($n = 3$ total images per group) of CD31 (green) and EMCN (red) with DAPI (blue) stained femur sections from 2 week-old *Robo1$^{+/+}$* and *Robo1$^{-/-}$* mice. Growth plate is marked with a dashed line. Scale bars, 100μm. Values represent mean ± s.e.m.; *$P < 0.05$ and ***$P < 0.001$ by an unpaired two-tailed Student's *t*-test in all panels.
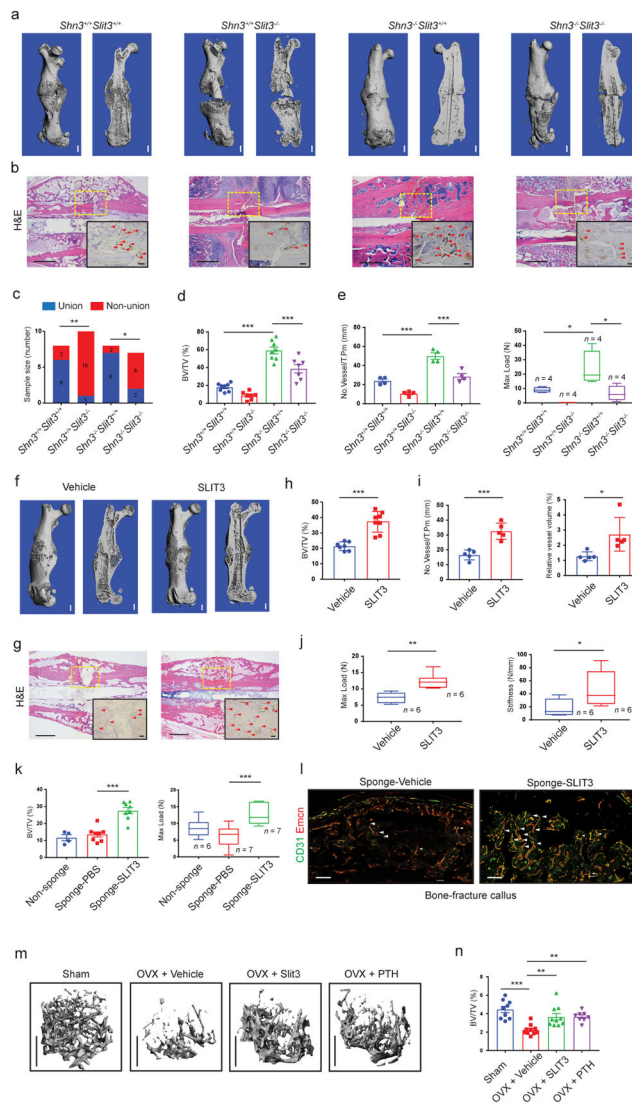
Figure 6.
Administration of recombinant SLIT3 has therapeutic effects on bone fracture healing and ovariectomy-induced bone loss. (**a**, **b**) Representative μCT (**a**), H&E staining (**b**) and EMCN immunohistochemistry (IHC) images (**b**, insert) (*n* = 4 total images per group) of mouse femurs 21 days after open femoral midshaft fracture. Dashed line boxes indicate the site of fracture. Arrowheads highlight EMCN positive vessels. Scale bar = 1 mm in μCT, 200μm in H&E and 100 μm in EMCN IHC. (**c–f**) Non-union frequency (**c**, *Shn3*^{+/+} *Slit3*^{+/+} = 8, *Shn3*^{+/+} *Slit3*^{−/−} = 11, *Shn3*^{−/−} *Slit3*^{+/+} = 8 and *Shn3*^{−/−} *Slit3*^{−/−} = 8), μCT measurement of BV/TV in callus area (**d**, *Shn3*^{+/+} *Slit3*^{+/+} = 8, *Shn3*^{+/+} *Slit3*^{−/−} = 7, *Shn3*^{−/−} *Slit3*^{+/+} = 8 and *Shn3*^{−/−} *Slit3*^{−/−} = 7), EMCN positive vessel numbers (**e**, left, *n* = 4 per group) and maximum compressive load (**e**, right, *n* = 4 per group) of the fractured femora 4 weeks after open femoral midshaft fracture. (**f–g**) Representative μCT (**f**), H&E staining (**g**) and EMCN IHC (**g**, insert) images (*n* = 4 total images per group) of mouse femurs 21 days post-fracture after IV injection of SLIT3 or PBS. Scale bar = 1 mm for μCT, 200 μm in H&E and100μm

in EMCN IHC. (**h–j**) μCT analysis of BV/TV in callus area (**h**, Vehicle = 7; SLIT3 = 8), EMCN positive vessel number and volume (**i**, $n = 5$ per group) and maximum compressive load and stiffness (**j**, $n = 5$ per group) of femurs 21 days after fracture with IV injection of SLIT3 or PBS. (**k**) Measurement of fracture callus BV/TV (left) and maximum load (right) of mouse femurs harvested 21 days post-fracture with insertion of a gelatin sponge soaked with SLIT3 or vehicle (BV/TV: Non-sponge = 4, Sponge-PBS = 8, Sponge-SLIT3 = 8; Maximum load: Non-sponge = 6, Sponge-PBS = 7, Sponge-SLIT3 = 7). (**l**) Representative confocal images ($n = 3$ total images per group) of CD31 (green) and EMCN (red) dual immunostained callus sections of mouse femurs 21 days post-fracture with insertion of a gelatin sponge soaked with SLIT3 or vehicle (high power, insert). Arrowheads highlight CD31^{hi}EMCN^{hi} vessels. Scale bars, 400μm. (**m, n**) Representative μCT images of the trabecular bone in the distal femur (**m**) and relative BV/TV (Sham = 9, OVX+Vehicle = 10, OVX+Slit3 = 9, OVX+PTH = 8). Scale bars, 1mm. Values represent mean ± s.e.m; *$P <$ 0.05, **$P <$ 0.01, ***$P <$ 0.001 by a Fisher's exact test (panel c) unpaired two-tailed Student's *t*-test or by one-way ANOVA followed by a Dunnett's test in all other panels.